Journal of Materials Research and Technology 27 (2023) 3531–3538

Contents lists available at ScienceDirect

Journal of Materials Research and Technology

journal homepage: www.elsevier.com/locate/jmrt

Promoting densification and grain growth of $BaCe_{0.65}Zr_{0.2}Y_{0.15}O_{3-\delta}$

Wenyu Zhou [a,c,*,1], Fanlin Zeng [a,**,1], Jürgen Malzbender [a], Hartmut Schlenz [a], Wendelin Deibert [a], Dmitry Sergeev [a], Ivan Povstugar [b], Ruth Schwaiger [a,d], Arian Nijmeijer [c], Michael Müller [a], Olivier Guillon [a,e], Wilhelm Albert Meulenberg [a,c]

[a] *Forschungszentrum Jülich GmbH, Institute of Energy and Climate Research (IEK), 52425, Jülich, Germany*
[b] *Forschungszentrum Jülich, Central Institute for Engineering, Electronics and Analytics (ZEA-3), 52425 Jülich, Germany*
[c] *Inorganic Membranes, MESA+ Institute for Nanotechnology, University of Twente, P.O. Box 217, 7500 AE, Enschede, the Netherlands*
[d] *RWTH Aachen University, Faculty 5, Chair of Energy Engineering Materials, 52056 Aachen, Germany*
[e] *Institute of Mineral Engineering Rheinisch-Westfälische Technische Hochschule (RWTH) Aachen University Mauerstraße 5, 52064 Aachen, Germany*

ARTICLE INFO

Keywords:
Proton conductor
Perovskite
NiO additive
Sintering
Densification
Grain growth

ABSTRACT

$BaCe_{0.65}Zr_{0.2}Y_{0.15}O_{3-\delta}$ (BCZ20Y15) has raised great interest due to its good protonic conductivity and chemical stability. However, the sintering of the material is considerably challenged by its refractory nature. In the current work, almost fully densified single-phase BCZ20Y15 with grain sizes exceeding 10 μm was successfully fabricated by sintering at 1500 °C by using calcined powders consisting of naturally separated perovskite phases and 0.5 wt % NiO. The role of NiO as sintering aid was elucidated by Inductively Coupled Plasma Optical Emission Spectroscopy (ICP-OES) and Atom Probe Tomography (APT) methods, concerning global and local material composition. Furthermore, the mechanism leading to the promoted densification and grain growth is elucidated based on current experimental results and a comprehensive review of the literature.

1. Introduction

$BaCeO_3$-based materials have raised considerable interest due to their high protonic conductivity [1–6], in particular when doped with 15 % Y [7,8]. Additional doping with more than 20 % Zr enhances the chemical tolerance against atmospheres containing CO_2, H_2O, and/or H_2S [9–13]. Hence, Y and Zr co-doped $BaCeO_3$ compounds, e.g. $BaCe_{0.65}Zr_{0.2}Y_{0.15}O_{3-\delta}$ (BCZ20Y15), have been developed and proved to be promising candidates for applications as membranes for hydrogen separation and electrolytes for intermediate-temperature solid oxide fuel cells [14–17]. In particular, BCZ20Y15 shows remarkably high H_2 permeance when combined with Gd-doped CeO_2 forming a dual-phase composite [17].

However, the Zr-doped $BaCeO_3$ compounds possess poor sinterability and high GB (grain boundary) resistance [18], which severely impeded their applications. The use of high sintering temperatures (1700 °C) and long annealing times (24 h + 6 h) can lead to full densification [19], but lead also to BaO vaporization, which impairs the performance (conductivity and stability) of the obtained material [14,20,21]. Thus, the processing challenges necessitate the use of sintering additives [18,22]. A widely studied sintering aid is NiO [18,23–28], which permits a decrease in the densification temperature to ~ 1400 °C [28,29]. NiO also contributes to enhanced grain growth. For instance, a grain size up to 10 μm has successfully been obtained for $BaZr_{0.5}Ce_{0.3}Y_{0.2}O_{3-\delta}$ with 1 wt% NiO addition at 1600 °C [30]. Such a large grain size significantly reduces the number of grain boundaries, and hence, improves the conductivity [30–32]. Nevertheless, a temperature of 1600 °C is still rather high, thus, the sample has to be covered completely with powder precursors to prevent or compensate for BaO loss [33]. Further reduction of the temperature to 1550 °C can eliminate the need to use a BaO-protective powder cover, but cannot realize a comparable grain size exceeding 10 μm [18,30], even for a sintering time of more than 20 h [31]. Furthermore, the evolution of the local chemistry within grains and the nanosized grain boundaries (regarding the width) following the large grain growth has not been well understood, which necessitates the utilization of high-resolution characterization methods, such as Atom Probe Tomography (APT).

In the current work, BCZ20Y15 with high density and grain sizes

---

[*] Corresponding author. Forschungszentrum Jülich GmbH, Institute of Energy and Climate Research (IEK), 52425, Jülich, Germany.
[**] Corresponding author.
E-mail addresses: w.zhou@fz-juelich.de (W. Zhou), f.zeng@fz-juelich.de (F. Zeng).
[1] These authors contributed equally: Wenyu Zhou and Fanlin Zeng.

https://doi.org/10.1016/j.jmrt.2023.10.180
Received 5 June 2023; Accepted 17 October 2023

exceeding 10 μm was successfully synthesized by a solid state reaction at a temperature of 1500 °C. A low amount of NiO was used as a sintering aid (0.5 wt%), and thus secondary phases were avoided after sintering. The chemical composition and distribution within the obtained large grains and in the vincintiy of the nanosized grain boundaries wrer characterized by APT, providing new insights into the mechanism that promotes densification and grain growth.

2. Experimental

BCZ20Y15 samples were prepared by a solid state reaction method (SSR). $BaCO_3$ (99 %, Sigma Aldrich), CeO_2 (99.9 %, Sigma Aldrich), ZrO_2 (99 %, Sigma Aldrich) and Y_2O_3 (99 %, Sigma Aldrich) were used as starting materials. Precursor powders were mixed (shaker mixer TURBULA T2, Willy A. Bachofen GmbH, Nidderau, Germany) in ethanol according to the stoichiometry for 24 h and the resultant mixtures were dried at 80 °C. Then, the BCZ20Y15 mixtures were calcined at 1150 °C for 6 h [14] and 1300 °C for 5 h [33]. 0.5 wt % NiO (99 %, Sigma Aldrich) was then added to the calcined powders as a sintering aid [34], and the obtained powder mixture was ball-milled (Rollermill RM1, Zoz GmbH, Wenden, Germany. ZrO_2 balls, 3.5 mm diameter, weight ratio powder: balls: ethanol = 1 : 2: 3) in ethanol for either 1 day or 7 days, respectively. Finally, the powder mixtures were dried and sieved through a 160 μm mesh.

Particle size distribution (PSD) of the meshed powders was measured by laser diffraction spectrometry (Horiba LA950-V2, Horiba Europe GmbH, Germany) and the specific surface area was measured via BET-method [35] by nitrogen adsorption at a temperature of −196 °C (AREAmeter II, Ströhlein Instruments, Germany).

Bulk membranes were obtained by uniaxially pressing the powders into a disc shape under a pressure of ~20 MPa for 5 min, yielding green samples with diameters and thicknesses of ~27 mm and ~1 mm, respectively. The green samples were sintered at 1500 °C for 5 h in air [33,34], and a constant heating/cooling rate of 5 K min^{-1} was used. Sintering behavior was characterized by a dilatometer (DIL 402 C Dilatometer, Netzsch-Gerätebau GmbH, Germany).

The crystal structure and phase purity of the sintered samples were characterized using an EMPYREAN (PANalytical) diffractometer with parafocusing Bragg-Brentano geometry, employing a Cu-LFF-tube (40 kV/40 mA), a BBHD mirror (Bragg-BrentanoHD mirror, manufactured by Malvern Panalytical, Ltd., Malvern, UK), 0.04 rad Soller slits, and a PIXcel3D detector. X-ray diffraction (XRD) patterns were recorded at room temperature using a step scan procedure (0.4 s per step, 0.013° per step size) in the 2θ range of 5–90°. The Rietveld refinement was conducted using the FullProf software package [36].

The microstructures and topographies of the samples were assessed by a Zeiss SUPRA 50VP field emission scanning electron microscope (SEM, Zeiss Microscopy GmbH, Oberkochen, Germany). The respective specimen for this test was first embedded in epoxy resin, ground sequentially using SiO_2 sandpaper with 400 and 2000 grit size and then polished using 6 μm, followed by a 1 μm, diamond suspension. The final polishing was conducted using 50 nm colloidal silica polishing suspension. The image analysis software Image J [37] was used to determine the grain sizes and porosity (estimated porosity = (pore area)/(whole area)*100 %. Different length-scales and different regions were analyzed to avoid bias from microstructure inhomogeneity.) from the backscattered scanning electron microscope (BSEM) micrograph.

The chemical composition of the sintered sample was determined using the inductively-coupled plasma optical emission spectroscopy (ICP-OES) with a device of Thermo Fisher Scientific (Germany).

Atom probe tomography (APT) specimens were prepared using a dual-beam focused-ion-beam (FIB) system (FEI Helios Nanolab 600i) by the conventional lift-out technique [38]. To reduce Ga implantation, a 2 keV Ga beam was used for the final shaping of APT tips. APT analyses were performed using a reflectron-equipped local electrode atom probe tool (LEAP 4000X HR, Cameca Instruments) in laser mode. Laser pulses of 355 nm wavelength, 12 ps pulse length, 30 pJ pulse energy and 200 kHz frequency were applied. The specimen base temperature was kept at 50 K and the ion detection rate was maintained at 0.01 ions per pulse. Data reconstruction and analysis were performed using Cameca IVAS 3.6.18 software package. Reconstruction parameters (evaporation field and image compression factor) were calibrated to match the specimen end radius and the length of the field-evaporated volume as measured by SEM before and after the APT run.

3. Results and discussion

3.1. Powder pre-treatment

After calcination at 1150 °C for 6 h, the mixed powders still contain at least 4 phases, including raw materials of CeO_2 and $BaCO_3$, as indicated by the XRD investigation in the supplementary Fig. S1. When the calcination temperature increases to 1300 °C, the powder mixtures are free of any kind of raw powders, but contain more than one perovskite phase (Fig. 1 (a)). These phases share overlapped peak positions, which cannot be precisely separated and quantified (Fig. 1(b)). Nevertheless, the upper and lower bounds of the compositions can be qualitatively (according to the peak positions) identified as $BaCe_{0.8}Y_{0.2}O_{3-\delta}$ (ICSD: 92261) and $BaZr_{0.885}Y_{0.115}O_{3-\delta}$ (ICSD: 8383), respectively. The $BaCe_{0.8}Y_{0.2}O_{3-\delta}$ phase possesses the highest intensities, and thus, represents the major phase, while $BaZr_{0.885}Y_{0.115}O_{3-\delta}$ is the minor phase with the lowest intensity. Intermediate phases are also presented, and their peak positions are between the ones of the major and the minor phase, but closer to the ones of the major phase. This indicates that the intermediate phases are also Ce and Y-rich perovskites and likely possess a small amount of Zr.

Although single-phase powders can be synthesized by additional calcination step(s) at the same or a high temperature [1,13,19,28, 39–42], the multiple-phase powders obtained here by the one-step calcination were not thermally treated further but directly used for sintering after NiO addition and ball milling. There are two reasons behind this: firstly, the use of a sintering temperature (1500 °C) that is higher than the calcination temperature will eventually ensure the forming of single-phase composition, so it is not necessary to pre-synthesize single-phase powder precursors via the multiple calcination steps; secondly, and more importantly, it is anticipated that the significant amount of Ce-rich and Zr-free perovskites in the powder precursors is a benefit for fast grain growth during sintering [3,39, 43–47], which will be discussed later in detail in section 3.4.

3.2. Sintering with NiO

0.5 wt% NiO as a sintering aid was added into the calcined powders before ball-milling to benefit material preparation. Further ball-milling was carried out to reduce the particle size and primary grain size, thus benefiting sintering [48–50]. Comparing the results after 1 day and 7 days of ball-milling, only a negligible difference could be observed regarding the particle size distributions (supplementary Fig. S2). However, the specific surface area of the powder after one week of ball-milling is ~4 m^2/g, which is significantly higher than the one (~1 m^2/g) after 24 h ball-milling. The higher specific surface area indicates a smaller primary particle size, implying a reduced necessary elemental diffusion distance and enhanced driving force during sintering, which will benefit the formation of single-phase BCZ20Y15 during sintering.

The uniaxially cold-pressed powders were then sintered at 1500 °C for 5 h, thus single-phase BCZ20Y15 was obtained, as verified by XRD (Fig. 2(a)). The Rietveld analysis yields the best calculation result ($\chi^2 = 2.21$, $R_{wp} = 8.64$) when the $BaCe_{0.65}Zr_{0.2}Y_{0.15}O_{3-\delta}$ (ICSD: 181962) with a space group of *I2/m* is used as the reference. This indicates that a single perovskite structure was obtained.

When NiO is used as a sintering aid, an emerging phase-BaY_2NiO_5 and residual NiO have been reported to exist in the sintered materials

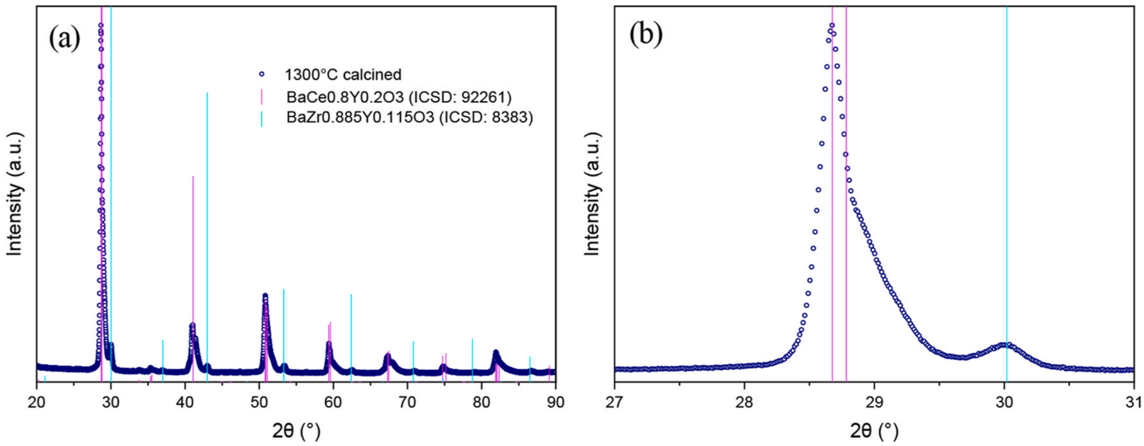

Fig. 1. XRD patterns of the mixed powders after 1300 °C/5 h calcination. (b) Represents the magnified 2θ angle range in (a) covering the peak with the highest intensity. The legends in (a) also apply to (b).

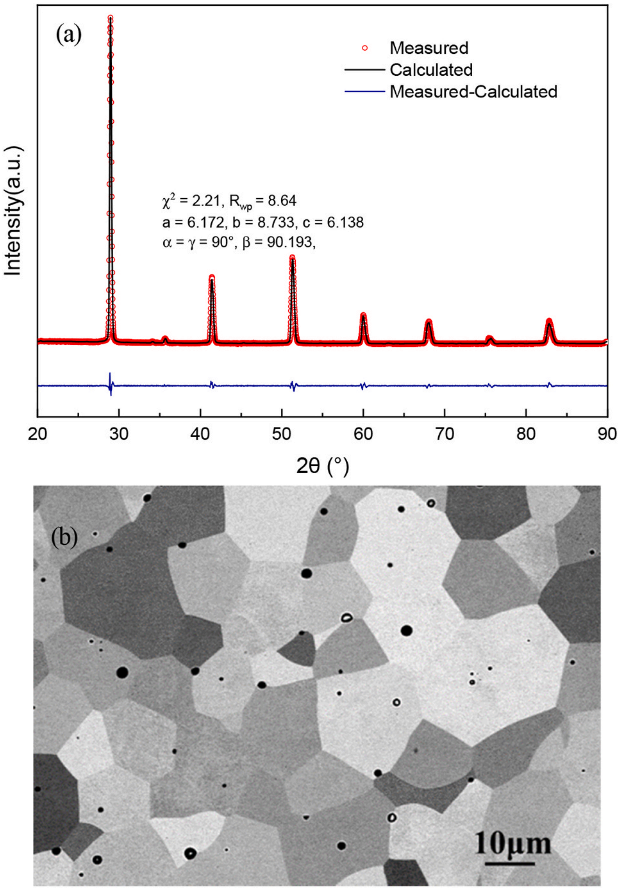

Fig. 2. Rietveld refined XRD pattern (a) and SEM microstructure (b) of the sample sintered at 1500 °C for 5 h (with 0.5 wt% NiO as sintering aid). The different contrasts in (b) indicate different crystal orientations. The black dots in (b) are pores.

[18,42,50,51], which is suggested to reduce the conductivity [28]. However, peaks related to potential phases in addition to the perovskites were not observed in the current XRD patterns, as shown in Fig. 1 as well as Fig. S3, indicating the secondary phase was eliminated successfully in this work.

The microstructure of the sintered sample shows significantly large grain sizes of ~13 μm and lower porosity (<1 %), as shown in Fig. 2(b). For protonic conducting material, the impedance at grain boundaries is usually several orders higher than the bulk conductivity [52]. Larger grain sizes and thus fewer grain boundaries will benefit the proton conduction [32]. Besides, also lower porosity indicates a larger effective area for proton conduction. Because of its microstructural characteristics, the material obtained here exhibits significant advantages for its application as a proton conducting membrane.

3.3. *Global and local chemistry*

The ICP-OES characterized elements concentration (Table 1) reveals that the overall actual stoichiometry of the sintered material is $Ba_{0.98}Ce_{0.67}Zr_{0.19}Y_{0.14}O_{3-\delta}$, which is close to the targeted one –$BaCe_{0.65}Zr_{0.2}Y_{0.15}O_{3-\delta}$. This indicates no substantial loss of Ba at the sintering temperature of 1500 °C. Besides that, the Ni content confirms that the addition of NiO is indeed ~0.5 wt%.

A complementary APT investigation was performed to elucidate the local chemistry of the grain bulk and boundary at a nanoscale. The GB within the pre-sharpened APT specimen is marked by the arrows in Fig. 3 (a). The 3D reconstructions of the cation distributions are displayed in Fig. 3(b–f)). At the GB, Y, Zr, and Ni are slightly enriched, while Ba is depleted. Ce shows a little degree of inhomogeneity across the GB. As quantitive information, the elemental relative concentration profiles across the GB were extracted from APT data and plotted in Fig. 3 (g, h). The substantial amount of Ni is detected within the grain bulk (see Fig. 3(h)), which indicates that Ni is doped into the perovskite crystal structure. Despite obvious variations of the cationic concentrations at the grain boundary, the observed elemental ratio does not correspond to any known side phases including the BaY_2NiO_5 phase, which has been reported as a potential secondary phase [28,30,51]. This suggests the absence of BaY_2NiO_5 as a second phase within the GB. However, it should be noted that although the absolute concentration values in the profiles are not accurate due to partially unresolved peak overlaps in the mass spectrum as well as certain APT artifacts, the relative bulk-to-grain boundary concentrational variations remain entirely correct.

The GB accumulation of Y has been also reported for $BaZrO_3$ doped with 6 % [53] and 10 % Y [54], while the GB depletion of Ba has been only reported for 6 % Sc-doped $BaZrO_3$ [53] but not for the Y-doped one [53,54]. For the $BaZrO_3$-based materials, Y as a dopant replaces Zr

Table 1
Elemental concentration of BCZ20Y15 characterized by ICP-OES.

	BCZ20Y15				
Probe	Ba	Ce	Zr	Y	Ni
Content [wt. %]	46.6 ± 1.6	32.4 ± 1.1	5.9 ± 0.2	4.3 ± 0.1	0.45 ± 0.01

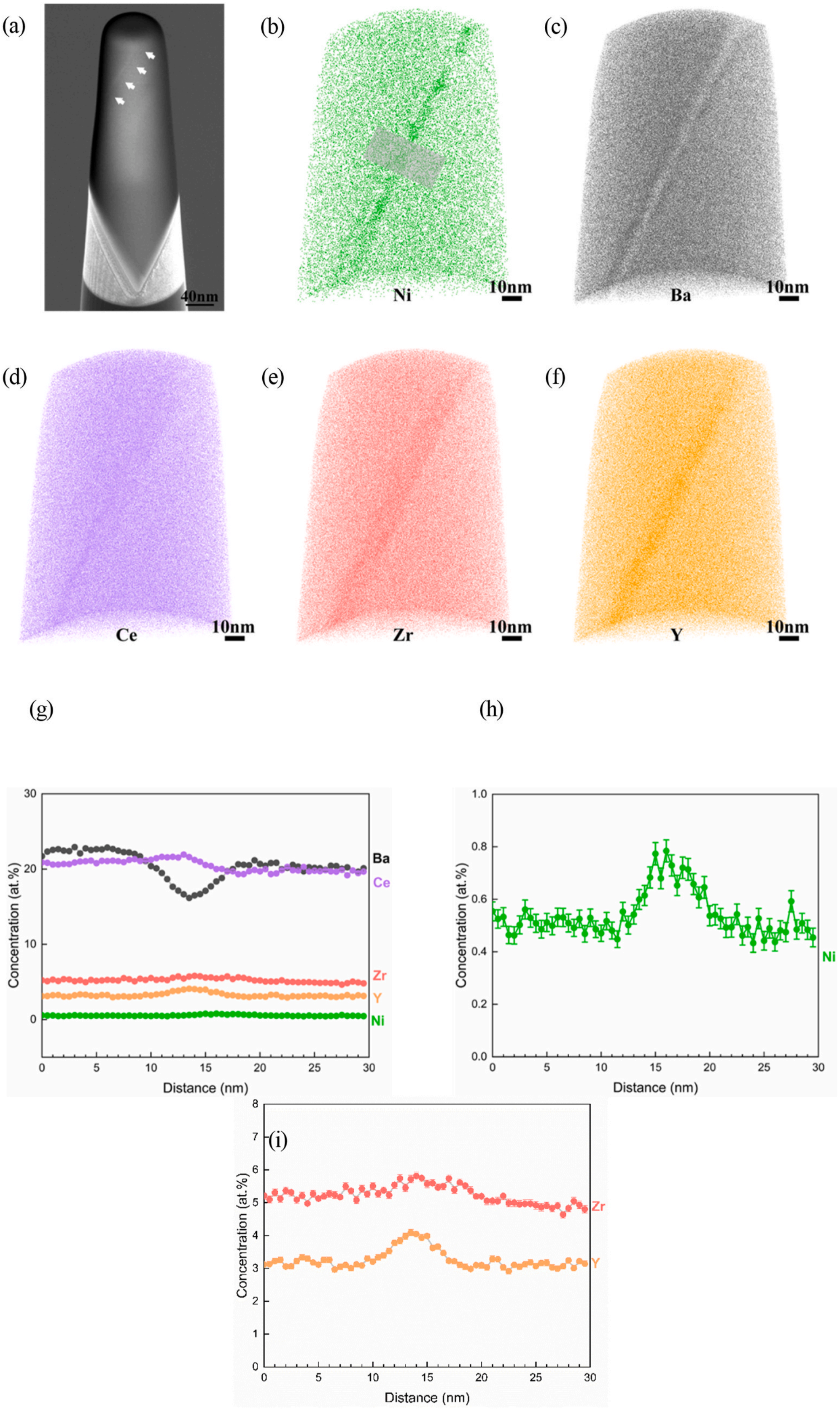

Fig. 3. APT analysis of a BCZ20Y15 specimen. (a) SEM of the pre-sharped APT specimen. The arrows mark the GB. (b) APT elemental maps for Ni, (c) Ba, (d) Ce, (e) Zr and (f) Y. (g) Elemental concentration profiles across the GB of the position marked in (b), and in particular zoomed-in (h) the Ni concentration profile and (i) Zr and Y profiles.

forming the negatively charged $[Y'_{Zr}]$ [55], the accumulation of which at the GB contributes to an improvement of the conductivity by reducing the space charge potential (or the width of the space charge layer) caused by the positively charged GB core [53,55,56]. Analogously, for $BaCeO_3$-based materials, $[Y'_{Ce}]$ tends to form when Y is introduced as a dopant. Hence, the GB accumulation of Y observed in our materials can benefit the conductivity. Besides, Ba depletion at the GB can also be an advantage for the conductivity, considering that Ba vacancies are likely negatively charged [53], which however needs further investigation in future studies.

3.4. Mechanism for promoting densification and grain growth

Several studies of the synthesis of doped barium zirconate/cerate materials already exist in the literature. One of the most widely used synthesis routines is the solid state reaction method, where $BaCO_3$ or $BaSO_4$, CeO_2, Y_2O_3, and/or ZrO_2 are used as the raw materials. The solid state reaction method is more environmentally friendly and cost-effective than the wet chemistry method [30,31]. Besides, it is also very feasible and promising for scale-up.

In a conventional solid state reaction (CSSR) process, the raw materials are calcined to completely remove raw materials and form the desired single-phase solid solution. In addition, a sintering aid will be added, if necessary, into the calcined powders before compacting and sintering. By contrast, in an “unconventional” solid state reaction method, i.e. the so-called solid state reactive sintering (SSRS), the calcination step is excluded and the ball-milled powder mixture of raw materials and sintering aid, e.g. NiO, is directly compacted for sintering [18,26,30,31,47,51,57].

The BCZ20Y15 in this work was prepared following the CSSR procedure, but the calcination step was “incomplete” since heterogeneous perovskites are present within the calcine. The sintering process of BCZ20Y15 involves complex phase evolution steps that can be analogous to those taking place during the SSRS process. Therefore, densification and grain growth behaviors observed here are compared with the reported ones from CSSR and SSRS.

3.4.1. Comparison with conventional solid state reaction (CSSR)

Table 2 displays a series of doped barium zirconate/cerate materials obtained by CSSR. Without sintering aid, Y-doped $BaCeO_3$ (Zr-free) materials generally possess much better sinterability (higher density and larger grain sizes at lower sintering temperatures) than Zr-doped $BaCeO_3$ materials. Furthermore, the grain growth is increased in the case of additional Y content for both Y-doped $BaCeO_3$ and Zr-doped $BaCeO_3$ materials. Besides, introducing Zr as a second dopant into the Y-doped $BaCeO_3$ significantly decreases the sinterability, which is closely correlated to the reduced Ce and Y concentrations. Therefore, the significant amount Zr-free and Y-rich Ba(Ce, Y)O_3 (likely $BaCe_{0.8}Y_{0.2}O_{3-\delta}$) as observed in our calcine (see Fig. 1) is a big advantage for densification due to its high intrinsic sinterability.

When NiO is added as a sintering aid, the sinterabilities of all Zr-containing materials are improved. The sinterability of BCZ20Y15 calcine with 0.5 wt% NiO in this work appears to be superior to other Zr-containing Ba(Ce, Y)O_3. An even better sinterability can be expected for the Zr-free Ba(Ce, Y)O_3 with NiO addition due to its high intrinsic sinterability, although there is currently, to the best of our knowledge, no available data as direct support.

Currently, there are two theories to explain the role of NiO during sintering. One theory assumes that Ni is accommodated on the B-site of the parent perovskite [47,58], i.e. doped into the crystal structure, which creates point defects and improves the diffusion leading to an enhanced sinterability [28,59,60]. The other one is a liquid phase sintering theory [18,61]. NiO induces phase reactions at ~800 °C yielding a new phase product of $BaNiO_x$, followed by another reaction at ~900 °C, obtaining then BaY_2NiO_5 [31]. The perovskite as a reactant with NiO is expected to experience an increase in cation vacancies due to the loss of Ba and Y [51]. The emerging $BaNiO_x$ phase exists in a narrow temperature range between 800 and 850 °C [31], whereas, BaY_2NiO_5 remains in a broad temperature range between 900 and 1500 °C [30,31]. BaY_2NiO_5 melts at 1450–1500 °C [31], and wets the solid grains, creating a capillary force that pulls the grains together. Thus, mass diffusion is facilitated in this liquid vessel, leading to grain coarsening at lower temperatures and for shorter sintering times [62].

The liquid phase sintering theory is well supported by the observation of BaY_2NiO_5 residue for the materials sintered below 1600 °C (see Table 2), except $BaCe_{0.35}Zr_{0.5}Y_{0.15}O_{3-\delta}$ and our BCZ20Y15. For the materials sintered at 1600 °C, the BaY_2NiO_5 residue appears to be absent, since BaY_2NiO_5 likely decomposes itself at ~1600 °C [30,31,63].

Interestingly, for materials sintered at 1500 °C, BaY_2NiO_5 is found for $BaCe_{0.5}Zr_{0.3}Y_{0.2}O_{3-\delta}$ with 1 wt% NiO addition [30], but not for our BCZ20Y15 with 0.5 wt% NiO addition. Similarly, Tong et al. [26] also observed BaY_2NiO_5 in $BaZr_{0.8}Y_{0.2}O_{3-\delta}$ samples sintered with 1 wt% and 2 wt% NiO at 1500 °C, but not in the one with 0.5 wt% NiO. Knight et al. [64] applied a fast quenching step as well as a slowly cooling step from 1500 °C for the $BaZr_{0.8}Y_{0.2}O_{3-\delta}$ samples sintered with 0.1–0.8 wt% NiO content, and detected a BaY_2NiO_5 phase for all quenched samples but not for the slow cooled ones. This indicates that, when the NiO addition is less than 1 wt%, BaY_2NiO_5 still forms in the sintering process but disappears later (likely dissolves into the perovskite crystal structure as maybe assumed from the APT results in Fig. 3) during slow cooling from 1500 °C.

Table 2
Ba(Ce, Y, Zr)O_3 synthesized by conventional solid state reaction (CSSR).

Material	NiO addition	Initial shrinking temperature	Final sintering conditions	Density [%]	Grain size [μm]	Secondary phase(s)	Ref.
$BaZr_{0.95}Y_{0.05}O_{3-\delta}$	–	–	1800 °C for 20 h	>95	0.67	–	[43,65]
$BaZr_{0.9}Y_{0.1}O_{3-\delta}$	–	–	1800 °C for 20 h	>95	1.4	–	[43]
	1 wt%	–	1600 °C for 10 h	96.5	1–4	–	[66]
$BaZr_{0.85}Y_{0.15}O_{3-\delta}$	–	–	1800 °C for 20 h	>95	2.7	–	[43]
$BaZr_{0.8}Y_{0.2}O_{3-\delta}$	–	–	1600 °C for 10 h	~100	1.4	–	[67]
	–	–	1500 °C for 24 h	97	0.7	–	[68]
$BaCe_{0.9}Y_{0.1}O_{3-\delta}$	–	–	1600 °C for 24 h	97.5	8–12	–	[69]
	–	–	1550 °C or 10 h	–	2.8	–	[70]
$BaCe_{0.8}Y_{0.2}O_{3-\delta}$	–	–	1550 °C or 10 h	–	4.5	–	[70]
$BaCe_{0.7}Zr_{0.1}Y_{0.2}O_{3-\delta}$	–	1150	1400 °C for 6 h	79.5	0.9	–	[28]
	0.5 wt%	1000	1400 °C for 6 h	98.7	3.6	BaY_2NiO_5	[28]
$BaCe_{0.6}Zr_{0.3}Y_{0.1}O_{3-\delta}$	–	–	1700 °C for 6 h	90–95	0.5–5	–	[39]
$BaCe_{0.5}Zr_{0.3}Y_{0.2}O_{3-\delta}$	–	–	1600 °C for 10 h	>95	1.5	–	[30]
	1 wt%	–	1600 °C for 10 h	>95	5	–	[30]
	1 wt%	–	1500 °C for 10 h	>97	3	BaY_2NiO_5	[30]
$BaCe_{0.35}Zr_{0.5}Y_{0.15}O_{3-\delta}$	–	1150	1700 °C for 10 h	>95	3–5	–	[42]
	4 mol.%	1000	1400 °C for 6 h	>95	3–5	NiO	[42]
$BaCe_{0.65}Zr_{0.2}Y_{0.15}O_{3-\delta}$	**0.5 wt%**	**800**	**1500 °C for 5h**	**> 99**	**13**	–	**This work**

However, for $BaCe_{0.7}Zr_{0.2}Y_{0.1}O_{3-\delta}$ with 0.5 wt% NiO sintered at 1400 °C, BaY_2NiO_5 is still present although no quenching step was applied [28]. Since the sintering temperature of 1400 °C is ~50 K lower than the melting temperature of BaY_2NiO_5, BaY_2NiO_5 likely exists in a mixed state of solid and liquid. The liquid fraction can easily dissolve into the surrounding perovskite particles due to the good contact, while the solid fraction cannot dissolve fast enough and remains after cooling. But it is not clear, for $BaCe_{0.35}Zr_{0.5}Y_{0.15}O_{3-\delta}$ with 4 mol.% NiO sintered at 1400 °C, why NiO is residual instead of BaY_2NiO_5.

Nevertheless, BaY_2NiO_5 is expected to form from the phase reactions between our BCZ20Y15 calcine and NiO, and it melts at the final sintering temperature (1500 °C), but disappears after cooling. The occurrence of the phase reactions is indicated by the decreased initial shrinking temperature after NiO addition, as shown in Table 2. The BCZ20Y15 calcine with 0.5 wt% in this work starts to shrink at ~800 °C (see Table 2 and Fig. 4), which is almost identical to the phase reaction temperature [31]. Whereas, the initial shrinking temperature is only reduced to ~1000 °C for $BaCe_{0.7}Zr_{0.1}Y_{0.2}O_{3-\delta}$ [28] and $BaCe_{0.35}Zr_{0.5}Y_{0.15}O_{3-\delta}$ by NiO addition, which can be attributed to the low sinterability of the material itself due to Zr incorporation as well as sluggish and hysteretic phase reactions, possibly caused by the Zr-stabilized perovskite structure. Presumably in low-temperature ranges (<1000 °C), the reaction in the current BCZ20Y15 calcine mainly initiates between NiO and the $Ba(Ce, Y)O_3$ (which possesses no Zr, and hence high intrinsic sinterability) phase component, which promotes the shrinkage. Despite the low reactivity with NiO below 1000 °C, the particles of other Zr-rich $Ba(Zr, Y)O_3$ phase components are likely to be compacted together by the surrounding particles of the $Ba(Ce, Y)O_3$ phase component. Above a certain temperature, the different perovskite phases are expected to be merged as one perovskite phase, and the role of NiO in this process will be discussed in the next section in comparison with SSRS.

3.4.2. *Comparison with solid state reactive sintering (SSRS)*

Table 3 lists several $Ba(Ce, Y, Zr)O_3$ materials synthesized by SSRS with 1 wt% NiO at sintering temperatures of 1500 °C or 1400 °C. The highest sinterability is observed for the $BaCe_{0.8}Y_{0.2}O_{3-\delta}$ with 1 wt % NiO addition, which coincides with our conclusions from CSSR that the Zr-free $Ba(Ce, Y)O_3$ composition will gain the largest promotion on sinterability by NiO addition. Besides, comparable sinterabilities are indicated for the Zr and Y co-doped $BaCeO_3$ during SSRS and CSSR with NiO addition, while better sinterability is shown for the BCZ20Y15 calcine with NiO addition in the current work. Besides, a BaY_2NiO_5 residue is generally found for the $Ba(Ce, Y, Zr)O_3$ materials with 20 %Y, while for the $Ba(Ce, Y, Zr)O_3$ materials with Y less than 20 %, BaY_2NiO_5 will not be residue and it is probably dissolved into perovskites. This reflects that the Y content, in addition to the NiO content as discussed in the previous section, also affects the presence of any BaY_2NiO_5 residue.

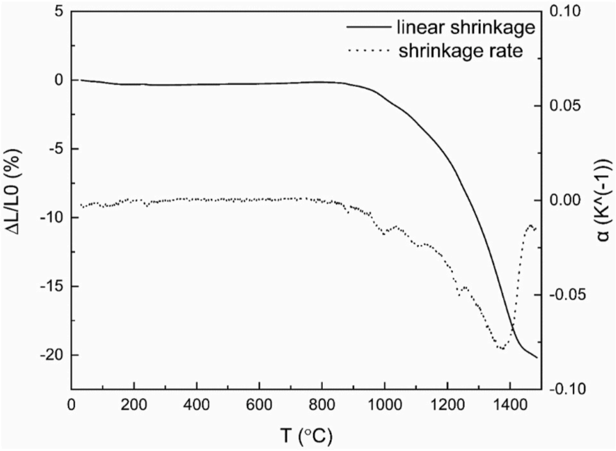

Fig. 4. Sintering behavior of the BCZ20Y15 calcine (with 0.5 wt% NiO addition).

During the SSRS process, raw materials disappear gradually and emerging phases including $BaNiO_x$, BaY_2NiO_5, and $Ba(Ce, Y, Zr)O_3$ perovskites appear successively above 800 °C [18,31]. The powder mixtures can approach a sintering stage that is analogous to the one in this work, where heterogenous perovskites with NiO are present. For instance, during the SSRS process of $Ba_{1.015}Zr_{0.664}Ce_{0.20}Y_{0.136}O_{3-\delta}$ with 0.5 wt % NiO, a nearly undoped $BaZrO_3$ phase and a Zr-free $Ba(Ce, Y)O_3$ phase form simultaneously at ~1000 °C [18], and merge into one single perovskite phase above 1400 °C. Further increasing the NiO content to 2 wt% is reported to decrease the formation temperature of the single perovskite phase by 50 K [18], which highlights the NiO contribution regarding uniforming perovskite phases. For comparison, the calcined powders in this work contain a similar phase component, i.e., the Zr-free $Ba(Ce, Y)O_3$ phase, but also a different one, i.e. the Y-doped $BaZrO_3$ instead of the undoped $BaZrO_3$ phase. A temperature below 1400 °C can be expected for the formation of a single perovskite phase in the calcined powders (with 0.5 wt % NiO) in this work, since the crystal structure discrepancy between the Zr-free $Ba(Ce, Y)O_3$ and the Y-doped $BaZrO_3$ is smaller than the one between the Zr-free $Ba(Ce, Y)O_3$ and the undoped $BaZrO_3$. Besides, this reduction is also contributed by the phase reactions between the Zr-free $Ba(Ce, Y)O_3$ and NiO starting at ~800 °C. The phase reactions possibly stimulate and/or promote complex cation/anion/defects diffusion between particles of different perovskites to construct a new stable perovskite structure in two ways: 1) increasing concentrations of cation vacancies in the Zr-free $Ba(Ce, Y)O_3$, and 2) initiating a shrinkage and reduction of the particle distance.

According to all discussions above, sinterability is verified to be superior for our BCZ20Y15 calcine after adding 0.5 wt% NiO in comparison to literature data. The superiority is attributed to the NiO addition as well as the presence of the Zr-free $Ba(Ce, Y)O_3$ phase as the major component in the BCZ20Y15 calcine. The Zr-free $Ba(Ce, Y)O_3$ phase possesses high sinterability. It likely reacts with NiO and initiates sintering of the BCZ20Y15 calcine at a temperature as low as 800 °C. It will merge with the minor Zr-rich $Ba(Zr, Y)O_3$ phase components forming a single-phase perovskite at a temperature lower than 1400 °C due to NiO. At the final sintering temperature of 1500 °C, the phase reaction product-BaY_2NiO_5 melts and significantly promotes densification and grain growth. The amount of BaY_2NiO_5 is low due to the low NiO addition (0.5 wt %) so the BaY_2NiO_5 likely dissolves completely into the perovskite crystal structure, instead of being a residue after sintering.

4. Conclusions

In the current work, a superior microstructure (density of >99 % and average grain size of ~13 μm) is obtained for the proton conducting ceramic BCZ20Y15 at a sintering temperature of 1500 °C. Although 0.5 wt% NiO is added as a sintering aid and the calcined powders possess heterogenous perovskite phases, no secondary phase impurities in addition to BCZ20Y15 perovskite are found according to XRD, SEM, and APT investigations. The superior sinterability is attributed to the NiO addition as well as the presence of a very sinterable phase (likely $BaCe_{0.8}Y_{0.2}O_{3-\delta}$) as the major component in the calcined powders. NiO starts to promote the sintering behavior of the calcine at a low temperature possibly by reacting with the abundant $BaCe_{0.8}Y_{0.2}O_{3-\delta}$ phase in the calcine. The phase reaction product (likely BaY_2NiO_5) melts and significantly promotes the densification and grain growth during the final sintering stage at 1500 °C. However, the BaY_2NiO_5 is not residual after sintering but likely dissolves into the perovskite crystal structure. Accumulation of Y and depletion of Ba at a grain boundary as shown by APT might contribute to the reduction of the space charge potential and an enhancement of the conductivity.

Table 3
Ba(Ce, Y, Zr)O_3 synthesized by solid state reactive sintering (SSRS) with 1 wt% NiO.

Material	Sintering	Density [%]	Grain size [μm]	Secondary phase(s)	Ref.
$BaZr_{0.9}Y_{0.1}O_{3-\delta}$	1500 °C for 4 h	98	1.3	Negligible	[57]
$BaZr_{0.8}Y_{0.2}O_{3-\delta}$	1500 °C for 24 h	95	5	BaY_2NiO_5	[26]
$BaCe_{0.8}Y_{0.2}O_{3-\delta}$	1400 °C for 12 h	98	>10	BaY_2NiO_5	[51]
$BaCe_{0.5}Zr_{0.3}Y_{0.2}O_{3-\delta}$	1500 °C for 10 h	>97	≥3	BaY_2NiO_5	[30]
$BaCe_{0.4}Zr_{0.5}Y_{0.1}O_{3-\delta}$	1500 °C for 4 h	98.2	3.3	Negligible	[57]
$Ba_{1.015}Zr_{0.664}Ce_{0.20}Y_{0.136}O_{3-\delta}$	1500 °C for 8 h	>95	2–3	No	[18]

Declaration of competing interest

The authors declare that they have no known competing financial interests or personal relationships that could have appeared to influence the work reported in this paper.

Acknowledgements

This work was supported by the China Scholarship Council (CSC). The authors would also like to thank especially Dr. E. Wessel, Dr. D. Grüner, Mr. M. Ziegner for the microstructural characterizations.

Appendix A. Supplementary data

Supplementary data to this article can be found online at https://doi.org/10.1016/j.jmrt.2023.10.180.

References

[1] Katahira K, Kohchi Y, Shimura T, Iwahara H. Protonic conduction in Zr-substituted BaCeO3. Solid State Ionics 2000;138(1):91–8.

[2] Ma X, Dai J, Zhang H, Reisner DE. Protonic conductivity nanostructured ceramic film with improved resistance to carbon dioxide at elevated temperatures. Surf Coating Technol 2005;200(5–6):1252–8.

[3] Sawant P, Varma S, Wani B, Bharadwaj S. Synthesis, stability and conductivity of BaCe0. 8− xZrxY0. 2O3− δ as electrolyte for proton conducting SOFC. Int J Hydrogen Energy 2012;37(4):3848–56.

[4] Yano M, Tomita A, Sano M, Hibino T. Recent advances in single-chamber solid oxide fuel cells: a review. Solid State Ionics 2007;177(39–40):3351–9.

[5] Radenahmad N, Afif A, Petra PI, Rahman SM, Eriksson S-G, Azad AK. Proton-conducting electrolytes for direct methanol and direct urea fuel cells–A state-of-the-art review. Renew Sustain Energy Rev 2016;57:1347–58.

[6] Phair J, Badwal S. Review of proton conductors for hydrogen separation. Ionics 2006;12(2):103–15.

[7] Kreuer K. Proton-conducting oxides. Annu Rev Mater Res 2003;33(1):333–59.

[8] Chiodelli G, Malavasi L, Tealdi C, Barison S, Battagliarin M, Doubova L, et al. Role of synthetic route on the transport properties of BaCe1− xYxO3 proton conductor. J Alloys Compd 2009;470(1–2):477–85.

[9] Fabbri E, D'Epifanio A, Di Bartolomeo E, Licoccia S, Traversa E. Tailoring the chemical stability of Ba (Ce0. 8− xZrx) Y0. 2O3− δ protonic conductors for intermediate temperature solid oxide fuel cells (IT-SOFCs). Solid State Ionics 2008;179(15–16):558–64.

[10] Magrez A, Schober T. Preparation, sintering, and water incorporation of proton conducting Ba0. 99Zr0. 8Y0. 2O3− δ: comparison between three different synthesis techniques. Solid State Ionics 2004;175(1–4):585–8.

[11] Tao S, Irvine JT. Conductivity studies of dense yttrium-doped BaZrO3 sintered at 1325 C. J Solid State Chem 2007;180(12):3493–503.

[12] Li J, Luo J-L, Chuang KT, Sanger AR. Chemical stability of Y-doped Ba (Ce, Zr) O3 perovskites in H2S-containing H2. Electrochim Acta 2008;53(10):3701–7.

[13] Ryu KH, Haile SM. Chemical stability and proton conductivity of doped BaCeO3–BaZrO3 solid solutions. Solid State Ionics 1999;125(1–4):355–67.

[14] Barison S, Battagliarin M, Cavallin T, Daolio S, Doubova L, Fabrizio M, et al. Barium non-stoichiometry role on the properties of Ba1+ xCe0. 65Zr0. 20Y0. 15O3–δ proton conductors for IT-SOFCs. Fuel Cell 2008;8(5):360–8.

[15] Barison S, Battagliarin M, Cavallin T, Doubova L, Fabrizio M, Mortalo C, et al. High conductivity and chemical stability of BaCe 1− x− y Zr x Y y O 3− δ proton conductors prepared by a sol–gel method. J Mater Chem 2008;18(42):5120–8.

[16] Doubova L, Barison S, Boldrini S, Fabrizio M, Mortalo C, Pagura C. Conductivity studies of sol-gel prepared BaCe 0.85− x Zr x Y 0.15 O 3− δ solid electrolytes using impedance spectroscopy. J Appl Electrochem 2009;39(11):2129–41.

[17] Rebollo E, Mortalo C, Escolástico S, Boldrini S, Barison S, Serra JM, et al. Exceptional hydrogen permeation of all-ceramic composite robust membranes based on BaCe 0.65 Zr 0.20 Y 0.15 O 3− δ and Y-or Gd-doped ceria. Energy Environ Sci 2015;8(12):3675–86.

[18] Huang Y, Merkle R, Maier J. Effects of NiO addition on sintering and proton uptake of Ba (Zr, Ce, Y) O3-δ. J Mater Chem A 2021;9(26):14775–85.

[19] Ricote S, Bonanos N, De Lucas MM, Caboche G. Structural and conductivity study of the proton conductor BaCe (0.9−x) ZrxY0. 1O (3− δ) at intermediate temperatures. J Power Sources 2009;193(1):189–93.

[20] Babilo P, Uda T, Haile SM. Processing of yttrium-doped barium zirconate for high proton conductivity. J Mater Res 2007;22(5):1322–30.

[21] Haile S, Staneff G, Ryu K. Non-stoichiometry, grain boundary transport and chemical stability of proton conducting perovskites. J Mater Sci 2001;36(5):1149–60.

[22] Loureiro FJ, Nasani N, Reddy GS, Munirathnam N, Fagg DP. A review on sintering technology of proton conducting BaCeO3-BaZrO3 perovskite oxide materials for Protonic Ceramic Fuel Cells. J Power Sources 2019;438:226991.

[23] Han D, Shinoda K, Tsukimoto S, Takeuchi H, Hiraiwa C, Majima M, et al. Origins of structural and electrochemical influence on Y-doped BaZrO 3 heat-treated with NiO additive. J Mater Chem A 2014;2(31):12552–60.

[24] Yoo C-Y, Yun DS, Joo JH, Yu JH. The effects of NiO addition on the structure and transport properties of proton conducting BaZr0. 8Y0. 2O3− δ. J Alloys Compd 2015;621:263–7.

[25] Kim E, Yamazaki Y, Haile S, Yoo H-I. Effect of NiO sintering-aid on hydration kinetics and defect-chemical parameters of BaZr0. 8Y0. 2O3− Δ. Solid State Ionics 2015;275:23–8.

[26] Tong J, Clark D, Hoban M, O'Hayre R. Cost-effective solid-state reactive sintering method for high conductivity proton conducting yttrium-doped barium zirconium ceramics. Solid State Ionics 2010;181(11):496–503.

[27] Polfus JM, Fontaine M-L, Thøgersen A, Riktor M, Norby T, Bredesen R. Solubility of transition metal interstitials in proton conducting BaZrO 3 and similar perovskite oxides. J Mater Chem A 2016;4(21):8105–12.

[28] Liu Z, Wang X, Liu M, Liu J. Enhancing sinterability and electrochemical properties of Ba(Zr0.1Ce0.7Y0.2)O3-δ proton conducting electrolyte for solid oxide fuel cells by addition of NiO. Int J Hydrogen Energy 2018;43(29):13501–11.

[29] Bu J, Jönsson PG, Zhao Z. Transport properties of BaZr0. 5Ce0. 3Y0. 2O3− δ proton conductor prepared by spark plasma sintering. Ceram Int 2016;42(3):4393–9.

[30] Bu J, Jönsson PG, Zhao Z. The effect of NiO on the conductivity of BaZr 0.5 Ce 0.3 Y 0.2 O 3− δ based electrolytes. RSC Adv 2016;6(67):62368–77.

[31] Tong J, Clark D, Bernau L, Sanders M, O'Hayre R. Solid-state reactive sintering mechanism for large-grained yttrium-doped barium zirconate proton conducting ceramics. J Mater Chem 2010;20(30):6333–41.

[32] Wang B, Bi L, Zhao XS. Exploring the role of NiO as a sintering aid in BaZr0.1Ce0.7Y0.2O3-δ electrolyte for proton-conducting solid oxide fuel cells. J Power Sources 2018;399:207–14.

[33] Zhou W, Malzbender J, Zeng F, Deibert W, Guillon O, Schwaiger R, et al. Mechanical properties of BaCe0. 65Zr0. 2Y0. 15O3-δ proton-conducting material determined using different nanoindentation methods. Journal of the European Ceramic Society; 2020.

[34] Zhou W, Malzbender J, Deibert W, Guillon O, Schwaiger R, Nijmeijer A, et al. High temperature compressive creep behavior of BaCe0. 65Zr0. 2Y0. 15O3-δ in air and 4% H2/Ar. Journal of the American Ceramic Society; 2021.

[35] Brunauer S, Emmett PH, Teller E. Adsorption of gases in multimolecular layers. J Am Chem Soc 1938;60(2):309–19.

[36] Rodríguez-Carvajal J. Recent advances in magnetic structure determination by neutron powder diffraction. Phys B Condens Matter 1993;192(1):55–69.

[37] Schneider CA, Rasband WS, Eliceiri KW. NIH Image to ImageJ: 25 years of image analysis. Nat Methods 2012;9(7):671–5.

[38] Thompson K, Lawrence D, Larson D, Olson J, Kelly T, Gorman B. In situ site-specific specimen preparation for atom probe tomography. Ultramicroscopy 2007;107(2–3):131–9.

[39] Ricote S, Bonanos N, Caboche G. Water vapour solubility and conductivity study of the proton conductor BaCe(0.9−x)ZrxY0.1O(3−δ). Solid State Ionics 2009;180(14):990–7.

[40] Zuo C, Zha S, Liu M, Hatano M, Uchiyama M. Ba(Zr0.1Ce0.7Y0.2)O3–δ as an electrolyte for low-temperature solid-oxide fuel cells. Adv Mater 2006;18(24):3318–20.

[41] Yang L, Zuo C, Liu M. High-performance anode-supported Solid Oxide Fuel Cells based on Ba(Zr0.1Ce0.7Y0.2)O3−δ (BZCY) fabricated by a modified co-pressing process. J Power Sources 2010;195(7):1845–8.

[42] An H, Shin D, Ji H-I. Effect of nickel addition on sintering behavior and electrical conductivity of BaCe0.35Zr0.5Y0.15O3-δ. J Korean Ceram Soc 2019;56(1):91–7.

[43] Iguchi F, Sata N, Tsurui T, Yugami H. Microstructures and grain boundary conductivity of BaZr1−xYxO3 (x=0.05, 0.10, 0.15) ceramics. Solid State Ionics 2007;178(7):691–5.

[44] Kim H-W, Seo J, Yu JH, Yun KS, Joo JH, Moon J, et al. Effect of cerium on yttrium-doped barium zirconate with a ZnO sintering aid: grain and grain boundary protonic conduction. Ceram Int 2021;47(23):32720–6.

[45] Zhong Z. Stability and conductivity study of the BaCe0.9−xZrxY0.1O2.95 systems. Solid State Ionics 2007;178(3):213–20.

[46] Nasani N, Dias PAN, Saraiva JA, Fagg DP. Synthesis and conductivity of Ba(Ce,Zr,Y)O3−δ electrolytes for PCFCs by new nitrate-free combustion method. Int J Hydrogen Energy 2013;38(20):8461–70.

[47] Nikodemski S, Tong J, O'Hayre R. Solid-state reactive sintering mechanism for proton conducting ceramics. Solid State Ionics 2013;253:201–10.

[48] M.N. Rahaman, Ceramic processing and sintering, CRC press2017.

[49] Jud E, Gauckler LJ. Sintering behavior of cobalt oxide doped ceria powders of different particle sizes. J Electroceram 2005;14(3):247–53.

[50] Yun DS, Kim J, Kim S-J, Lee J-H, Kim J-N, Yoon HC, et al. Structural and electrochemical properties of dense yttria-doped barium zirconate prepared by solid-state reactive sintering. Energies 2018;11(11):3083.

[51] Tong J, Clark D, Bernau L, Subramaniyan A, O'Hayre R. Proton-conducting yttrium-doped barium cerate ceramics synthesized by a cost-effective solid-state reactive sintering method. Solid State Ionics 2010;181(33):1486–98.

[52] Yamazaki Y, Hernandez-Sanchez R, Haile SM. High total proton conductivity in large-grained yttrium-doped barium zirconate. Chem Mater 2009;21(13):2755–62.

[53] Shirpour M, Rahmati B, Sigle W, van Aken PA, Merkle R, Maier J. Dopant segregation and space charge effects in proton-conducting BaZrO3 perovskites. J Phys Chem C 2012;116(3):2453–61.

[54] Clark DR, Zhu H, Diercks DR, Ricote S, Kee RJ, Almansoori A, et al. Probing grain-boundary chemistry and electronic structure in proton-conducting oxides by atom probe tomography. Nano Lett 2016;16(11):6924–30.

[55] Uthayakumar A, Pandiyan A, Krishna Moorthy SB. Yttrium dependent space charge effect on modulating the conductivity of barium zirconate electrolyte for solid oxide fuel cell. Int J Hydrogen Energy 2018;43(52):23488–99.

[56] Uthayakumar A, Pandiyan A, Mathiyalagan S, Keshri AK, Krishna Moorthy SB. The effect of space charge on blocking grain boundary resistance in an yttrium-doped barium zirconate electrolyte for solid oxide fuel cells. J Phys Chem C 2020;124(10):5591–9.

[57] Ricote S, Bonanos N, Manerbino A, Coors WG. Conductivity study of dense BaCexZr(0.9−x)Y0.1O(3−δ) prepared by solid state reactive sintering at 1500 °C. Int J Hydrogen Energy 2012;37(9):7954–61.

[58] Costa R, Grünbaum N, Berger M-H, Dessemond L, Thorel A. On the use of NiO as sintering additive for BaCe0, 9Y0, 1O3− α. Solid State Ionics 2009;180(11–13):891–5.

[59] Yu F, Xiao J, Lei L, Cai W, Zhang Y, Liu J, et al. Effects of doping alumina on the electrical and sintering performances of yttrium-stabilized-zirconia. Solid State Ionics 2016;289:28–34.

[60] Li S, Wang L. Special ceramic technology, vol. 132. Wuhan: Wuhan Institute of Technology Press; 1990.

[61] Huang Y, Merkle R, Maier J. Effect of NiO addition on proton uptake of BaZr1-xYxO3-x/2 and BaZr1-xScxO3-x/2 electrolytes. Solid State Ionics 2020;347:115256.

[62] German RM, Suri P, Park SJ. Liquid phase sintering. J Mater Sci 2009;44(1):1–39.

[63] Han D, Otani Y, Noda Y, Onishi T, Majima M, Uda T. Strategy to improve phase compatibility between proton conductive BaZr0.8Y0.2O3−δ and nickel oxide. RSC Adv 2016;6(23):19288–97.

[64] Knight M, Jennings D, Ricote S, Reimanis I. Estimating Ni valence with magnetometry in solid-state reactive sintered yttrium-doped barium zirconate. J Am Ceram Soc 2022;105(1):159–68.

[65] Iguchi F, Yamada T, Sata N, Tsurui T, Yugami H. The influence of grain structures on the electrical conductivity of a BaZr0.95Y0.05O3 proton conductor. Solid State Ionics 2006;177(26):2381–4.

[66] Ricote S, Bonanos N, Manerbino A, Sullivan NP, Coors WG. Effects of the fabrication process on the grain-boundary resistance in BaZr0.9Y0.1O3−δ. J Mater Chem A 2014;2(38):16107–15.

[67] Wendler LP, Ramos K, Souza DMPF. Investigation about the reason of limited grain growth of Y-doped barium zirconate. Ceram Int 2019;45(15):19120–6.

[68] Goulart CA, Boas LAV, Morelli MR, Souza DPFd. Reactive sintering of yttrium-doped barium zirconate (BaZr0.8Y0.2O3-δ) without sintering aids. Ceram Int 2021;47(2):2565–71.

[69] Lacz A. Effect of microstructure on chemical stability and electrical properties of BaCe0.9Y0.1O3 − δ. Ionics 2016;22(8):1405–14.

[70] Park ET, Goretta KC, de Arellano-López AR, Guan J, Balachandran U, Dorris SE, et al. High-temperature deformation of BaCe1−xYxO3−y (0.05≤x≤0.2). Solid State Ionics 1999;117(3):323–30.